Tellus SERIES A DYNAMIC METEOROLOGY AND OCEANOGRAPHY
PUBLISHED BY THE INTERNATIONAL METEOROLOGICAL INSTITUTE IN STOCKHOLM

Tellus (2011), 63A, 687–706
Printed in Singapore. All rights reserved

TELLUS

A continuous buoyancy based convection scheme: one- and three-dimensional validation

By J. F. GUÉRÉMY*, *Météo-France, Centre National de Recherches Météorologiques (CNRM), 42 av. G. Coriolis, 31057 Toulouse, France*

(Manuscript received 20 April 2010; in final form 28 February 2011)

ABSTRACT

A new and consistent convection scheme, providing continuous treatment of this atmospheric process, is described. The main concept ensuring the consistency of the whole system is buoyancy, a key element of any convective vertical motion. The buoyancy constitutes the forcing term of the convective vertical velocity, which is then used to define the triggering condition, the mass flux and the rates of entrainment–detrainment. The buoyancy is also used in its vertically integrated form to express the closure condition as a CAPE relaxation. The continuous treatment of convection from dry thermals to deep precipitating cumulus is made possible through the use of a continuous formulation of the entrainment–detrainment rates and CAPE relaxation time, together with an embedded precipitation scheme. This convection scheme is first evaluated with the help of single-column model simulations of specific case studies encompassing a variety of convective situations. Second, a coupled general-circulation model multiyear simulation is provided as a means to assess the model climate with respect to observations.

1. Introduction

The convection scheme is a key element of large-scale models. It is necessary because it is designed to represent processes occurring at scales much smaller than that of the processes resolved by the large-scale model. Furthermore, the subgrid-scale processes parametrized by this scheme, together with the vertical diffusion scheme, constitute the basis of the atmospheric response to the radiative forcing. These processes include both transport and water phase changes.

Such schemes have been developed since the beginning of large-scale modelling (Arakawa, 2004). The first and most simple was the moist convective adjustment scheme (e.g. Manabe et al., 1965). Since then, convection schemes have gained in complexity. Most of the present convection schemes use a mass flux concept (e.g. Bougeault, 1985; Tiedtke, 1989; Gregory and Rowntree, 1990; Kain and Fritsch, 1990; Emanuel, 1991; Zhang and McFarlane, 1995).

The aim of this paper is to describe a new mass flux convection scheme based principally on bringing together rather simple, already published ideas in a consistent way. The main concept ensuring the consistency of the whole system is the buoyancy, a key element of any convective vertical motion. The buoyancy constitutes the forcing term of the convective vertical velocity, which in turn will later be found everywhere else in the algorithm of the convection scheme (i.e. in the mass flux, the rates of entrainment–detrainment, the triggering and closure conditions), ensuring its consistency. Another key originality of this scheme is its ability to represent all types of convection in a continuous manner, from dry thermals to deep precipitating convective systems, with the help of an embedded precipitation scheme and a continuous formulation of both entrainment–detrainment rates and closure condition. Other convection schemes including buoyancy as central aspects of their formulation have already been developed (e.g. Anthes, 1977; Donner, 1993; Bretherton et al., 2004; Nober and Graf, 2005). This scheme is quite close to that of Bretherton et al. (2004) in its design in that a single bulk plume is considered instead of an ensemble as in Donner (1993) or Nober and Graf (2005). It could be seen as an extension of that of Bretherton et al. (2004), being developed to represent convective processes beyond shallow convection in a continuous way. Moreover, in this scheme, the convective vertical velocity is computed using a time-dependent equation (instead of steady-state) in an attempt to introduce more memory into the system, and the entrainment–detrainment rates are defined using this convective vertical velocity as input (instead of the inverse of the convective top height) in order to obtain a local reinforced link to the buoyancy.

This new scheme has been implemented in the general-circulation model (GCM), called ARPEGE-Climat (AC, Gibelin

*Correspondence.
e-mail: jean-francois.gueremy@meteo.fr
DOI: 10.1111/j.1600-0870.2011.00521.x

and Déqué, 2003), and used in climate research at Météo-France. This model can be used either in a single-column model (SCM) mode or in a GCM mode.

Section 2 is devoted to the description of the convection scheme. The validation of the scheme is presented in Section 3, where both SCM and GCM simulation results are shown.

2. Description of the scheme

2.1. Large-scale convection tendencies

The large-scale convection tendencies for heat, moisture and momentum are the following:

$$\left(\frac{\partial \bar{e}}{\partial t}\right)_c = -\frac{\partial \overline{\omega' e'}}{\partial p} + LC, \tag{1}$$

$$\left(\frac{\partial \bar{q}}{\partial t}\right)_c = -\frac{\partial \overline{\omega' q'}}{\partial p} - C, \tag{2}$$

$$\left(\frac{\partial \bar{u}}{\partial t}\right)_c = -\frac{\partial \overline{\omega' u'}}{\partial p} + \mathrm{PGE}, \tag{3}$$

$$\left(\frac{\partial \bar{v}}{\partial t}\right)_c = -\frac{\partial \overline{\omega' v'}}{\partial p} + \mathrm{PGE}, \tag{4}$$

where $e = C_p T + gz$ is the dry static energy, q the specific humidity, u and v the two components of the horizontal velocity, ω the vertical p velocity, and C the net rate of condensation. The subscript c denotes the contribution from cumulus convection. The overbar denotes averages over a horizontal area that is large enough to contain an ensemble of clouds, and the prime denotes deviations from the horizontal average. PGE stands for the effect of the pressure gradient (between the convective ascent and its environment). Vertical eddy fluxes include many scales, but only the convective scale is considered here, the turbulent scale being taken into account by the vertical diffusion scheme. The horizontal eddy flux divergences are neglected. Following the work of Yanai et al. (1973), the convection tendencies mentioned above can be expressed in another way. Let χ be any of the prognostic fields considered. Its average can be written as

$$\bar{\chi} = \alpha\sigma\,\chi_c + (1 - \alpha\sigma)\,\chi_e, \tag{5}$$

where α is a constant, σ the normalized convective fractional area coverage (function of p, starting from 1 at convection base and decreasing above, simulating an ensemble of convective plumes whose depths decrease with height). The subscript c denotes the convective quantity, and e the environmental quantity. Taking the Reynolds conditions into account, the vertical eddy flux is given by

$$\overline{\omega' \chi'} = \overline{\omega\chi} - \bar{\omega} \cdot \bar{\chi}. \tag{6}$$

Substituting (5) into (6), we obtain

$$\overline{\omega' \chi'} = \alpha\sigma\,(\omega_c - \omega_e)\,(\chi_c - \bar{\chi})\,. \tag{7}$$

Using the justified assumption $|\omega_c| \gg |\omega_e|$ (e.g. Yanai et al., 1973), (7) can be written as

$$\overline{\omega' \chi'} = -M\,(\chi_c - \bar{\chi})\,, \tag{8}$$

where $M = -\alpha\sigma\omega_c$ is the mass flux (the reason for this 3-factor formulation is discussed at the beginning of the next subsection). Following the work of Yanai et al. (1973), the stationarized equations of a cumulus ensemble bulk model (cumulus ensemble budgets of mass, heat, moisture and momentum) are

$$\frac{\partial M}{\partial p} = D - E, \tag{9}$$

$$\frac{\partial M e_c}{\partial p} = D e_c^d - E\bar{e} - LC, \tag{10}$$

$$\frac{\partial M q_c}{\partial p} = D q_c^d - E\bar{q} + C, \tag{11}$$

$$\frac{\partial M u_c}{\partial p} = D u_c - E\bar{u} - PGE, \tag{12}$$

$$\frac{\partial M v_c}{\partial p} = D v_c - E\bar{v} - PGE, \tag{13}$$

where D and E are the rates of mass detrainment and entrainment per unit pressure interval. The exponent d signifies the value in the detraining air. Equations (10)–(13) have been written assuming the well-justified approximation $\chi_e = \bar{\chi}$, implying that $\alpha \ll 1$ (e.g. Yanai et al., 1973). Using eq. (8)–(13), the initial set of equations (1)–(4) giving the convection tendencies can be rearranged in the following manner:

$$\left(\frac{\partial \bar{e}}{\partial t}\right)_c = -M\frac{\partial \bar{e}}{\partial p} + D\left(e_c^d - \bar{e}\right), \tag{14}$$

$$\left(\frac{\partial \bar{q}}{\partial t}\right)_c = -M\frac{\partial \bar{q}}{\partial p} + D\left(q_c^d - \bar{q}\right), \tag{15}$$

$$\left(\frac{\partial \bar{u}}{\partial t}\right)_c = -M\frac{\partial \bar{u}}{\partial p} + D\,(u_c - \bar{u})\,, \tag{16}$$

$$\left(\frac{\partial \bar{v}}{\partial t}\right)_c = -M\frac{\partial \bar{v}}{\partial p} + D\,(v_c - \bar{v})\,. \tag{17}$$

The first terms on the right-hand sides of (14)–(17) represent the cumulus-induced subsidence of the surrounding air, and the second terms the effects of detrainment of cloud properties in the surrounding air. This classical set of equations, obtained with the following three assumptions: $|\omega_c| \gg |\omega_e|$, $\alpha \ll 1$ and stationary convective variables, is used in this scheme. At this stage, expressions for the mass flux M, the detrainment D and the bulk cloud profile remain to be defined.

2.2. Cloud model and closure condition

One of the main novel aspects of this scheme is the algorithm used to compute the mass flux M. At each level of the vertical grid, the convective vertical velocity ω_c is computed first, followed by the normalized convective fractional area coverage σ [with the help of the mass budget (9)], the convective magnitude given by the constant α not being required at this stage of the algorithm. Finally, the constant α that completely defines M [i.e. eq. (8)] is obtained with the closure condition expressed as a vertically integrated equation. The details of this process as a whole will be given below. Only the updraught will be considered here, for the sake of simplicity and because the downdraught is processed in a second stage (see Section 2.3).

Following the work of Tiedtke (1989), entrainment E and detrainment D are decomposed into two parts corresponding to the two different scales at which these processes occur.

$$E = E_o + E_t, \quad D = D_o + D_t. \tag{18}$$

The first part, called the organized entrainment and detrainment (subscript o), corresponds to the mixing due to the flow associated with mesoscale convergence and divergence. The second part, called the turbulent entrainment and detrainment (subscript t), consists of the mixing due to turbulent exchanges of mass through cloud edges. The turbulent entrainment and detrainment rates are assumed to be equal as proposed by Tiedtke (1989). Fractional entrainment and detrainment rates (both organized and turbulent) can be defined following Turner (1963) as

$$E = M\varepsilon, \quad D = M\delta. \tag{19}$$

The bulk cloud profile is defined, starting from the bottom of the atmosphere, by considering layers encompassed between two variable levels. The first step consists of computing the effect of entrainment on the cloud variables over the considered layer.

$$\frac{\partial \chi_c}{\partial \phi} = (\varepsilon_t + \rho\varepsilon_o)(\bar{\chi} - \chi_c), \tag{20}$$

where χ is the temperature, the specific humidity or the components of the horizontal velocity. In the last case, the pressure gradient effect between the cloud and its environment is taken into account following Kershaw and Gregory (1997). The convective horizontal velocity components are then fully defined given their value at the base of the convective ascent (obtained with an additional condition of momentum conservation by the convective process over its entire depth). Equation (20) is solved numerically by considering the entire right-hand side taken at the bottom level, where all variables are already known; this can be justified by the fact that the entrainment process deals with the properties of air parcels at the base of the lifting ascent. The computation of the fractional entrainment rates will be presented later. Adiabatic processes then affect thermodynamic variables. Both dry (starting from the absolute temperature) and moist (starting from the wet bulb temperature) adiabats are considered; the choice between them will be made by comparing the temperatures at the top level [if the moist adiabat temperature is higher than that of the dry adiabat, the lifting condensation level (LCL) is located in the present layer], thus allowing an internal adaptive treatment of dry and moist ascent. The equations are the following:

$$C_p dT + d\phi = 0, \quad C_p dT + d\phi + L dq = 0, \tag{21}$$

that is, the classical conservation of dry and moist static energy over the layer considered. Equation (21) is discretized following Geleyn et al. (1994). Convective cloud water content is then diagnosed at the top variable level using the following equation:

$$\frac{\partial (q_c + q_{lc})}{\partial \phi} = -\frac{q_{lc}}{\phi_0}, \tag{22}$$

where ϕ_0 is a precipitating cloud critical geopotential thickness, corresponding to 800 m in this version of scheme. Equation (22) is an approximation of the stationary total water budget for the cloud (e.g. Arakawa and Schubert, 1974).

The values of dry static energy and specific humidity in the detraining air used in (14) and (15) are computed with the help of a neutral buoyancy condition, following Nordeng (1994):

$$\frac{1}{\bar{T}}\left(T_c^d - \bar{T}\right) + 0.608\left(\mathrm{qsat}(T_c^d) - \bar{q}\right) - q_{lc} = 0,$$
$$q_c^d = \mathrm{qsat}(T_c^d). \tag{23}$$

The convective vertical velocity is then computed following Simpson and Wiggert (1969) and Chen and Bougeault (1992) as

$$\frac{\partial \omega_c}{\partial t} = -\frac{1}{2}\frac{\partial \omega_c^2}{\partial p} - \frac{\rho g^2}{(1+\gamma)}\frac{\left(T_{vc} - \bar{T}_v\right)}{\bar{T}_v} + \left(\frac{\varepsilon_t}{\rho} + \varepsilon_o + K_d\right)\omega_c^2, \tag{24}$$

where $T_{vc} = T_c(1 + 0.608q_c - q_{lc})$ is the cloud virtual temperature, $\bar{T}_v = \bar{T}(1 + 0.608\bar{q})$ the grid averaged virtual temperature, γ a virtual mass parameter ($\gamma = 0.5$, e.g. Simpson, 1971) and K_d an aerodynamic drag parameter. This convective vertical velocity is the only convective variable obtained with a prognostic equation, similarly to the turbulent kinetic energy used in the associated vertical diffusion scheme (Cuxart et al., 2000), providing a memory effect in the convective process. Equation (24) is solved on the top variable level to obtain the cloud vertical velocity on the flux level just above the previous one (the cloud vertical velocity on the variable level being equal to half the value from the two adjacent flux levels). In the vertical direction, the starting value is set to zero but a function of the turbulent kinetic energy could be defined, namely in the case of a sequential physics implementation (parallel physics being considered here). An implicit time discretization is used following Chen and Bougeault (1992), so that the cloud vertical velocity (pressure coordinate) is obtained as the negative root of a second-order polynomial.

The cloud vertical velocity being obtained on the top variable level of the layer considered, the turbulent fractional entrainment

rate is defined on that level as

$$\varepsilon_{\rm t} = \varepsilon_{\rm tn} + (\varepsilon_{\rm tx} - \varepsilon_{\rm tn})\, f_\varepsilon(\omega_{\rm c}, \omega_{\rm cx}, \omega_{\rm cn}), \tag{25}$$

where $\varepsilon_{\rm tn}$ is a minimum value ($\varepsilon_{\rm tn} = 0.5 \times 10^{-4}\,{\rm m}^{-1}$), $\varepsilon_{\rm tx}$ is a maximum value ($\varepsilon_{\rm tx} = 11 \times 10^{-4}\,{\rm m}^{-1}$), $f_\varepsilon(\omega_{\rm c}, \omega_{\rm cx}, \omega_{\rm cn})$ is an analytical monotonic function of $\omega_{\rm c}$ which is equal to 1 when $\omega_{\rm c} \geq \omega_{\rm cx}$ ($\omega_{\rm cx} = -2\,{\rm Pa\,s}^{-1}$), and to 0 when $\omega_{\rm c} \leq \omega_{\rm cn}$ ($\omega_{\rm cn} = -38\,{\rm Pa\,s}^{-1}$); f_ε is a sine squared in this version of the scheme. Equation (25) allows both shallow and deep convection to be handled, providing a large value of entrainment for shallow convective ascent (small absolute value of p vertical velocity) and a small value of entrainment for deep convective ascent (large absolute value of p vertical velocity), as proposed by Tiedtke (1989) for example, but using a continuous transition in this scheme. The aerodynamic drag parameter $K_{\rm d}$ is computed on the top variable level in the same manner as for the fractional entrainment rate using a minimum value of $3.0 \times 10^{-4}\,{\rm m}^{-1}$, the maximum value being 22 times larger (the same factor as for the fractional entrainment rate).

The expression of the organized entrainment and detrainment rates was designed partly following the work of Bretherton et al. (2004). It is based on a buoyancy-sorting approach assuming that the lateral mixing of the updraught and its environment generates a spectrum of mixtures. Buoyancy sorting is used to determine which mixtures are incorporated into the updraught and which are rejected. First, a maximum value of the fractional entrainment–detrainment rate is defined as

$$(\varepsilon\delta)_{\rm ox} = \left| \frac{1}{\omega_{\rm c}} \frac{\partial \omega_{\rm c}}{\partial p} \right|. \tag{26}$$

This value is directly obtained from eq. (9) assuming a constant a priori zero value of $\delta_{\rm o}$ (before buoyancy sorting) when $\frac{\partial \omega_{\rm c}}{\partial p} > 0$ (increase of z-convective vertical velocity with z), and an a priori zero value of ε_o (before buoyancy sorting) and σ constant with height when $\frac{\partial \omega_c}{\partial p} < 0$ (decrease of z-convective vertical velocity with z). Bretherton et al. (2004) have defined the mass-mixing fraction of environmental air in the mixtures (hereafter called μ), ranging from 0 for undiluted updraught to 1 for pure environmental air. The value μ_0 partitioning positively versus negatively buoyant mixtures is computed from

$$T_{\rm vm}(\mu_0) = \bar{T}_{\rm v}, \tag{27}$$

where $T_{\rm vm}$ is the virtual temperature of the mixture, which is a piece-wise linearly mixing quantity (Bretherton et al., 2004). Given this critical mixing fraction, the net amount of surrounding air entrained in the updraught is

$$2\,(\varepsilon\delta)_{\rm ox}\, M \int_0^{\mu_0} \mu\, f_\mu(\mu)\, {\rm d}\mu = (\varepsilon\delta)_{\rm ox}\, M \mu_0^2, \tag{28}$$

where the factor 2 is due to the fact that equal parts of updraught and surrounding air are involved in the mixing process and f_μ is the mass-mixing probability function corresponding to an assumed uniform distribution. A similar relation is used for the updraught air being detrained after mixing, so that the fractional entrainment and detrainment rates are finally

$$\varepsilon_{\rm o} = (\varepsilon\delta)_{\rm ox}\, \mu_0^2, \quad \delta_o = (\varepsilon\delta)_{\rm ox}\, (1 - \mu_0)^2\,. \tag{29}$$

In order to take into consideration the fact that some negatively buoyant parcels are not immediately rejected from the updraught, this buoyancy-sorting scheme is not applied as long as the maximum fractional organized entrainment is significantly larger than its turbulent counterpart, that is,

$$-\frac{1}{\omega_{\rm c}} \frac{\partial \omega_{\rm c}}{\partial p} > K_\varepsilon \varepsilon_{\rm t}, \tag{30}$$

where K_ε is a constant ($K_\varepsilon = 2.5$, as empirically obtained with the help of SCM simulations).

Given the fractional entrainment and detrainment rates at the top variable level and the convective vertical velocity on the next flux level, the normalized convective fractional area coverage is computed, on the same level as the vertical velocity, using (9), as

$$\frac{1}{\sigma\omega_c} \frac{\partial \sigma \omega_c}{\partial p} = \delta_o - \varepsilon_o. \tag{31}$$

At this stage of the algorithm, the convective instability condition (triggering condition) of the layer under consideration is simply determined by the sign of the convective vertical velocity at both flux levels surrounding the top variable level. If the sign is negative (corresponding to an ascent) at least at one of the two flux levels, the layer is declared convectively unstable. If this is the case, the whole process is iterated for the following layer, and if not, the top level cloud temperature and humidity are reinitialized to the mean temperature and humidity before iterating. In order to take only non-local tropospheric convective processes into account, no convection is considered if the updraught starting level is located above the level of minimum equivalent potential temperature.

Everything needed to compute the convective tendencies (14)–(17) is thus known, except the constant α, which completely defines the mass flux (eq. 8). This constant is determined with the help of the closure condition based on a Convective Available Potential Energy (CAPE) relaxation approach. CAPE is classically defined as

$$\begin{aligned} {\rm CAPE} &= \int_b^t \frac{g}{\bar{T}_{\rm v}} \left(T_{\rm vc} - \bar{T}_{\rm v}\right) {\rm d}z, \ \text{or} \\ {\rm CAPE} &= \int_t^b R_{\rm d} \left(T_{\rm vc} - \bar{T}_{\rm v}\right) \frac{{\rm d}p}{p}, \end{aligned} \tag{32}$$

where the bounds t and b of the vertical integral stand for the top and the bottom, respectively, of the convective depth, being the successive convectively unstable layers, and $R_{\rm d}$ is the dry air gas constant. The closure condition is written as

$$\left(\frac{\partial {\rm CAPE}}{\partial t}\right)_{\rm c} = -\frac{\rm CAPE}{\tau}, \tag{33}$$

where the left-hand side term is the time derivative of CAPE due to convection, which is expanded using (32) to

$$\left(\frac{\partial \mathrm{CAPE}}{\partial t}\right)_{\mathrm{c}} = -R_{\mathrm{d}} \int_t^b \left((1+0.608\bar{q})\left(\frac{\partial \bar{T}}{\partial t}\right)_{\mathrm{c}} + 0.608\bar{T}\left(\frac{\partial \bar{q}}{\partial t}\right)_{\mathrm{c}}\right)\frac{\mathrm{d}p}{p}, \tag{34}$$

the term $(\frac{\partial T_{\mathrm{vc}}}{\partial t})_{\mathrm{c}}$ being neglected as in Nordeng (1994), basically because this convective scheme has been designed under the assumption of stationary convective variables in the time step. Equation (33) becomes a linear equation of α, substituting (14) and (15) into (34). The time response τ, during which convection consumes the pre-existing CAPE, is proportional to a ratio of a length (here, the convective depth) over a velocity (here, the mean vertical velocity in the convective depth). This internally computed characteristic time of the convective overturning allows the convective process to be treated continuously. The proportionality is defined with a linear function of the inverse of the resolution (i.e. linear function of the grid size) in order to keep the same magnitude between the mass flux and the resolved vertical velocity, which is itself proportional to the resolution (through the continuity equation). Thus, τ is expressed as

$$\tau = f_\tau(\mathrm{resolution})\frac{\left(\int_t^b \mathrm{d}p\right)^2}{\int_t^b |\omega_{\mathrm{c}}|\,\mathrm{d}p}. \tag{35}$$

Such a formulation for the time response τ has also been proposed in Bechtold et al. (2008).

The value of α computed from (33) is finally bounded by a maximum value of 0.1 in order to fulfil the basic assumption of negligible convective fractional area coverage.

2.3. Downdraughts

Cumulus-scale downdraughts are taken into account in this scheme. The tendencies of prognostic variables due to the downdraughts are identical to the set of eqs (14)–(17). The resulting effects correspond to a cooling due to the cumulus-induced ascent of surrounding air and the detrainment process, and to a moistening due to the cumulus-induced ascent of surrounding air and drying due to the detrainment process in the lower levels.

The definition of the downdraught profile is very similar to that for the updraught. The bulk profile is defined starting from the top of the updraught with a saturated parcel having the thermodynamic properties of the environmental air (wet bulb properties). If this starting level is located below the level of minimum equivalent potential temperature (consistently with what is done for the updraught), no downdraught is considered. In most cases, the downdraught starting level is actually the level of minimum equivalent potential temperature. Entrainment is taken into account with eq. (20), using a turbulent entrainment rate equal to $\varepsilon_{\mathrm{tx}}$ and an organized entrainment rate defined with a value of μ_0 equal to 1 if the p vertical downdraught velocity increases with the pressure, and 0 otherwise (corresponding to a constant value of the downdraught fractional area coverage). Moist adiabatic subsidence is considered until the updraught LCL is reached, where the dry adiabat takes over. The vertical downdraught velocity is computed using the steady-state version of eq. (24). The downdraught triggering condition is the same as the one for the updraught (with a change of sign). The same value of $\alpha\sigma$ obtained for the updraught is used to obtain the downdraught mass flux. Recognizing that the downdraught takes its energy from the evaporation of convective rain or condensate over a fractional area coverage $\alpha\sigma/4$ (only one-fourth of the convective area is assumed to be affected by the evaporation process, according to single-column simulations), the downdraught mass flux is multiplied again by this value. Thus, the final value of the downdraught mass flux is equal to the opposite of the p vertical downdraught velocity times $(\alpha\sigma)^2/4$.

2.4. Convective cloud fraction and precipitation

The convective cloud fraction (i.e. where convective cloud water is present), C_{c}, ranges between 0 and 1 and is proportional to the convective fractional area coverage (i.e. where upward and downward convective velocities are maximum) as

$$C_{\mathrm{c}} = K_{\mathrm{cc}}\alpha\sigma, \tag{36}$$

where K_{cc} is a constant disposable parameter ($K_{\mathrm{cc}} = 6.5$ in this version of scheme, obtained with the help of single-column simulations).

Suspended convective cloud condensate is set to be equal to the diagnosed convective cloud condensate defined with (22) (multiplied by $\alpha\sigma$ to obtain a value at grid-scale).

The convective precipitation flux is currently computed using a scheme proposed by Smith (1990). This scheme provides the tendencies of cloud condensate (liquid and solid) due to the precipitation process. These tendencies are expressed as functions of the cloud condensate itself. The cloud condensate to be considered here (q_{lc}^*) as an input to the precipitation scheme is the equilibrium cloud condensate $\alpha\sigma q_{\mathrm{lc}}$ in addition to what has been condensed (or evaporated) by the convective process during the time step.

$$q_{\mathrm{lc}}^* = \alpha\sigma q_{\mathrm{lc}} + C\Delta t, \tag{37}$$

where Δt is the time step. The net rate of condensation C is computed using (2) and (8), having obtained the q convective tendency from (15). For the sake of simplicity, an abrupt transition is assumed between solid and liquid cloud condensate at 0°C. Liquid cloud condensate evolution includes auto-conversion [with an exponential factor controlling conversion inhibition when the cloud condensate becomes small (allowing non-precipitating shallow convection)] and accretion processes. The auto-conversion characteristic time is determined by closing

the global mean atmospheric water budget over several annual cycles (i.e. surface precipitation equal to surface evaporation). The solid cloud condensate tendency is expressed as

$$\frac{P}{\rho \Delta z} - \frac{v_{\mathrm{F}}}{\Delta z} q^*_{\mathrm{lci}}, \tag{38}$$

where Δz is the layer thickness, P the frozen precipitation falling into the layer, v_{F} the fall-out speed and q_{lci} the solid cloud condensate. The fall-out speed is parametrized as in Liu and Orville (1969).

$$v_{\mathrm{F}} = K_{\mathrm{v}} \left(1000 \times \frac{q^*_{\mathrm{lci}}}{\alpha \sigma} \right)^{0.2}, \tag{39}$$

where K_v is a disposable parameter ($K_v = 1.0$ in this version of scheme).

The evaporation of convective rain is parametrized following Kessler (1969) where the evaporation is assumed to be proportional to the saturation deficit. Since the convective rain occurs only over a fraction of the grid area, $\alpha\sigma$ was naturally chosen but one-fourth of it is considered (accounting for the part of the convective area affected by the precipitation, as for the downdraughts). Moreover, this evaporation process is only taken into account below the LCL.

2.5. *Effects of convection on the mean cloud condensate*

The mean cloud condensate in a grid mesh is obtained from the turbulence scheme (super-saturation modified by the intensity of turbulence, Cuxart et al., 2000). Convection affects this variable through compensating vertical motion and detrainment. The former process is represented by the following term (e.g. (14)–(17)):

$$-M \frac{\partial \bar{q}_{\mathrm{l}}}{\partial p}, \tag{40}$$

where M is the total mass flux (updraught and downdraught) and $\bar{q}_{\mathrm{l}}$ the mean cloud condensate. In this version of the scheme, the detrained updraught convective condensate is assumed to evaporate during the time step (as in Yanai et al., 1973). Therefore, the updraught detrainment terms of (14) and (15) become

$$D\left(e^d_{\mathrm{c}} - \bar{e} - L\left(q_{\mathrm{lc}} - \bar{q}_{\mathrm{l}}\right)\right) \text{ and } D\left(q^d_{\mathrm{c}} - \bar{q} + q_{\mathrm{lc}} - \bar{q}_{\mathrm{l}}\right). \tag{41}$$

The properties of the convective clouds are combined with that of the mean clouds (obtained from the turbulence scheme) as the input to the radiation scheme. The combination assumes maximum overlapping of both cloud types over each layer, with the total cloud fraction and cloud condensate being the maximum value of the two cloud fractions and grid-scale condensates, respectively.

3. Validation of the scheme

Parametrizations have been generally evaluated in SCM mode using observational data, and in a fully prognostic three-dimensional framework. Evaluation in SCM mode has been carried out using prognostic tests: performing long-term integrations with specified forcing and analysing the predicted evolution of temperature and humidity (e.g. Betts and Miller, 1986). Furthermore, in recent years, SCM simulations have been evaluated against large-eddy simulation (LES) model runs (Bretherton et al., 2004), or cloud-resolving model (CRM) runs (Bechtold et al., 2000), in addition to actual observations. The advantage of using such explicit model runs is that they provide quantities that cannot be measured with the required precision, like the area covered by convective updraughts and downdraughts, and entrainment–detrainment rates. Prognostic SCM tests, in spite of their shortcomings (no feedback with the environment through horizontal advections), allow a detailed evaluation of parametrizations against observations and explicit simulations, and should be considered as a necessary but not sufficient assessment step. Therefore, there is a need for a fully prognostic three-dimensional framework to complete the assessment procedure (e.g. Tiedtke, 1989; Gregory and Rowntree, 1990). This second step could be achieved by simulating one or more three-dimensional case studies (as is done in a forthcoming paper) and/or by simulating a longer period to reach a climatic state. The latter approach was chosen in this work.

3.1. *SCM results*

Four cases were chosen for this paper. For the purpose of verifying deep penetrative convection, we used one tropical case from the TOGA-COARE data set (Jorgensen et al., 1997) and, for shallow convection, one trade wind cumulus case from the BOMEX data set (Nitta and Esbensen, 1974). Finally, the case set up by Guichard et al. (2004) from an original Atmospheric Radiation Measurement (ARM) case-study (Xie et al., 2002) provided an opportunity to evaluate the convective scheme over an entire continental diurnal cycle (from the build-up of the dry boundary layer in the morning to deep precipitating convection in the afternoon).

The SCM was the one-dimensional version of the GCM, called AC, used in climate research at Météo-France. The radiative scheme is derived from Morcrette (1990) and is activated every 3 h. The vertical diffusion at the surface is computed using the turbulence scheme of Louis (1979). The vertical diffusion scheme is a prognostic turbulent kinetic energy scheme (Cuxart et al., 2000). The stratiform precipitation is computed with the help of a scheme developed by Lopez (2002), with the cloud condensate provided by the vertical diffusion scheme as input, and cloud and precipitating water being treated as prognostic variables. In SCM mode, there are no horizontal advections of cloud and precipitating water because no such forcings are provided. The vertical discretization includes 91 levels defined by the European Centre for Medium Range Forecasts, notably including 8 levels below 500 m, which seems to be important to obtain a correct simulation of the lower part of the boundary

layer. A time step of 10 min is considered, which is used in GCM mode at low horizontal resolution (310 km).

The TOGA-COARE case is a 100-km-long oceanic squall line, with a broad stratiform precipitation region behind the convective leading edge, observed on 22 February 1993. The environment of the convective system has been described in the form of a composite sounding derived from both rawinsonde observations and aircraft data. This sounding, used as initial condition for the SCM and CRM simulations, is characterized by moderate instability and a very moist environment (relative humidity around 90% between the surface and 5 km). These thermodynamic conditions are thought to be representative of the environment of many tropical oceanic convective systems. A reference CRM simulation, labelled RSI3D in Redelsperger et al. (2000), was used both to compute the SCM forcings and to evaluate the SCM simulation, as in Bechtold et al. (2000). The time series of temperature and specific humidity forcings associated with the domain-averaged flow (100 × 125 km) in the reference CRM simulation were computed and time averaged over 1 h, over the 7-h period of that simulation. Initially, the forcing tendencies were weak, but the system quickly developed between 3 and 6 h and became quasi-stationary during the last hour, with maximum tendencies of –110 K d^{-1} and 25 g kg^{-1} d^{-1} in the mid-troposphere. At each time step, the two horizontal components of the wind were set to their initial values. The surface pressure, and sea surface temperature and specific humidity were kept constant with values of 1006 hPa, 301.3°K and 23.2 g kg^{-1}, respectively. The size of the CRM domain was taken into account in the definition of the convective time response, following (35).

Because the convective system reached a quasi-stationary state after 5 h, vertical profiles representing time averages over the last hour of simulation will be shown next. Considering (14)–(17), the convective tendencies are directly proportional to the convective mass flux M, apart from regions with strong detrainment. Therefore, the convective mass flux appears to be a key variable in the convection scheme evaluation process. Figure 1 shows the convective mass fluxes of both the CRM and SCM runs over the last hour of simulation. These mass fluxes include both the updraught and downdraught contributions. There is good agreement between the two curves, except above 6000 m, where the CRM mass flux is larger. This discrepancy might be due to the criterion used to define the mass flux in the CRM as, in these upper layers, mostly saturated stratiform processes take place. Those processes are simulated in the SCM by the resolved dynamics and the vertical diffusion scheme. Moreover, the present SCM mass flux profile appears to be among the best ones in fig. 5(b) of Bechtold et al. (2000).

What really matters is the evolution of the model state variables, which are determined by the time-integrated tendencies resulting from small differences between the forcing tendencies and the parametrized apparent sources. Therefore, the temperature and moisture differences of the SCM run with respect to

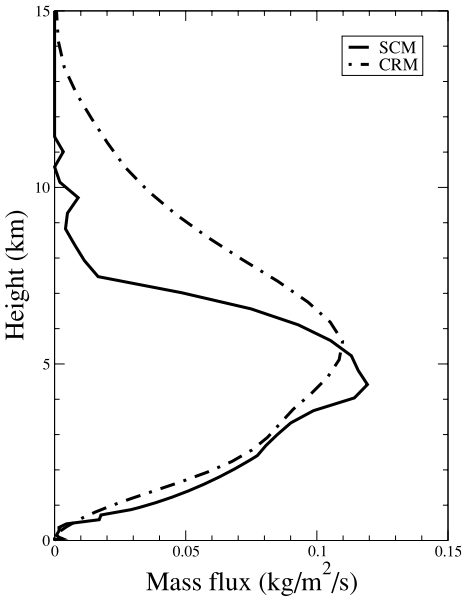

Fig. 1. Convective mass fluxes of both the CRM and SCM runs over the last hour of simulation.

CRM runs are depicted in Fig. 2, for the last hour of simulation. Concerning the temperature, an overall negative bias is apparent in Fig. 2(a). This negative bias is partly due to the fact that the SCM simulations use forcings computed from CRM for which the convection has been initiated artificially. Therefore, the convective evolution is delayed in the SCM simulations, giving rise to this negative bias. The bias reaches its maximum just above 4000 m, where the updraught mass flux is maximum. It is worth noting that the temperature bias is negative around 11 500 m as a result of a lesser extent of the convection in the SCM versus the CRM, which appears to be the case of other SCM simulations as shown in fig. 6(a) of Bechtold et al. (2000). Concerning the specific humidity, a consistent overall bias with the temperature is observed (i.e. positive bias) in Fig. 2(b). Along the vertical, the bias seems to be shifted towards the top compared to the temperature. Below 7000 m, the vertical profile presents three extrema, starting with a positive bias around 2000 m, followed by a negative one around 4000 m and a positive one at 7000 m; this vertical pattern is very similar to the one depicted in fig. 6(b) of Bechtold et al. (2000). Figure 2(b) also shows the same vertical profile of the humidity bias but for the SCM simulation without downdraughts. The largest impact of the downdraughts is located near the surface where the drying effect is clearly seen (bias of 0.5 g per kilogram with the downdraughts vs. 0.7 g per kilogram without). Aloft, a light moistening effect appears above 1500 m.

The shallow convection case selected was the period from 22 to 26 June 1969, part of phase 3 of BOMEX, during which no precipitating shallow cumuli were observed. Following the work of Siebesma and Cuijpers (1995), hereafter called SC95, a

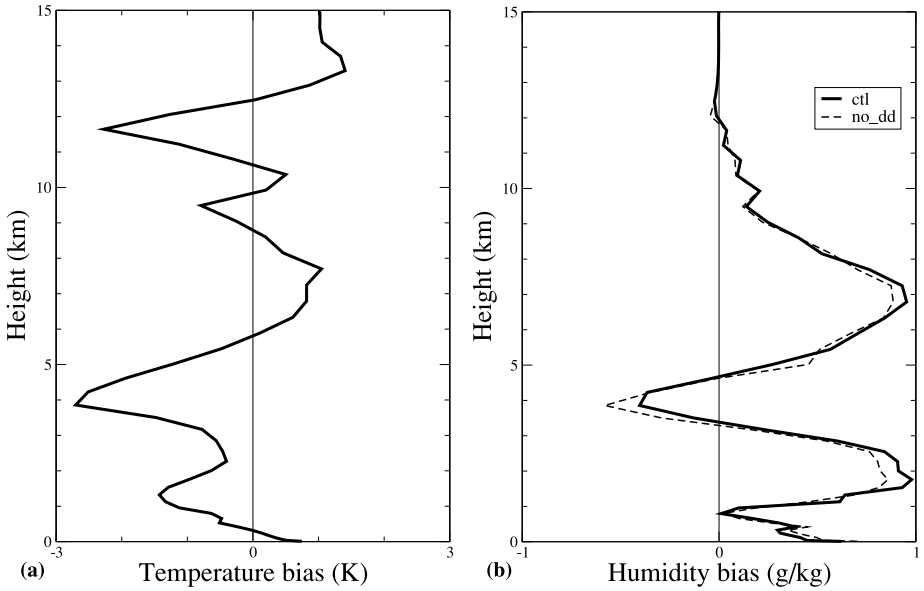

Fig. 2. Biases of temperature (a) and moisture (b) of the control SCM run, together with an SCM run without downdraughts, over the last hour of simulation.

mean profile was used as the initial condition (shown in Fig. 4). This profile was determined from an average over 22nd and 23rd June, during which a well-defined steady state with a strong inversion (between 1500 and 2000 m) was present over the whole BOMEX square (500×500 km^2). The stationary adiabatic forcings and radiative cooling (up to –2 K d^{-1}) are those defined in SC95. The most important adiabatic forcing is the subsidence between 2000 m and the surface, with a maximum of 0.65 cm s^{-1} (absolute value) at 1500 m. At each time step, the two horizontal components of the wind were computed using their time evolution equations given the geostrophic wind provided in SC95. The surface pressure, and sea surface temperature and specific humidity were kept constant with values of 1015 hPa, 300.4 K and 22.45 g kg^{-1}, respectively. The size of the BOMEX square was taken into account in the definition of the convective time response, following (35).

Figure 3(a) shows the time evolution of the simulated cloud fraction over a 24-h period. After a 5-h spin-up, a stationary shallow cumulus is obtained with a cloud base at 500 m and a cloud top reaching 1900 m, in agreement with the observation and LES runs (Siebesma et al., 2003). The cloud fraction decreases with height from about 30% to less than 10%, once again in accordance with what has been observed. Figure 3(b) shows the same time evolution of the simulated cloud fraction, but obtained with the 31-level version of the SCM. This coarser resolution includes only 3 levels below 500 m, which appears to be insufficient to accurately locate the LCL. The cloud base is definitely too low, and the shallow cloud is not able to spread over a proper depth. A vertical resolution including at least 2.5 times as many points (i.e. around 80 m layer depth below 500 m) is necessary to correctly simulate the dry layer under the cloud, and then the cloud itself.

A period of 19 h between 5 h and 24 h was considered to compute time average variables of this shallow cumulus. First of all, the vertical profile of the potential temperature (resp. specific humidity), at the beginning of the simulation and 24 h later, is depicted in Fig. 4(a) (resp. Fig. 4(b)). This case study is considered to be stationary (the physics should balance the prescribed dynamical forcings), as mentioned previously. The simulation provides fairly reasonable stationary behaviour as shown in Fig. 4. However, the moisture profile tends to be too dry just above the cloud base. This discrepancy is due to an underestimation of the moistening around the cloud base as presented in Fig. 5(b). In this critical layer, the moistening due to detrainment is just enough to overcome the significant drying due to condensation. There is also a tendency to underestimate the moistening at the top of cloud, but this might be due to a stronger inversion in the initial profile coming from the northern side of the BOMEX square compared to what existed in the observations covering the whole square, as pointed out in SC95 (Fig. 4). There is good agreement between the simulated apparent heat source and the observed one as shown in Fig. 5(a). This term does not include the radiative effect because it is taken into account in the prescribed forcings (–2 K d^{-1} below 1500 m). At the top of the cloud, the cooling due to detrainment (evaporation of cloud droplets) is underestimated, but for the same reasons as for the specific humidity.

The agreement in the apparent heat source and moisture sink and, in turn, in the simulated vertical profile, are of course a consequence of the rather good reproduction of both mass flux

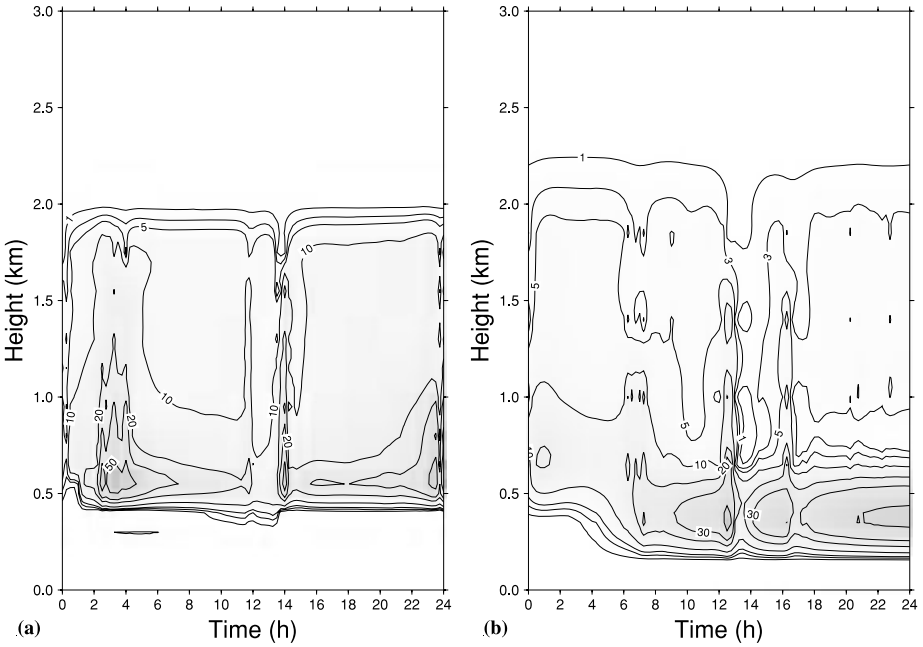

Fig. 3. Cloud fraction time evolution of SCM runs with 91 levels (a) and 31 levels (b).

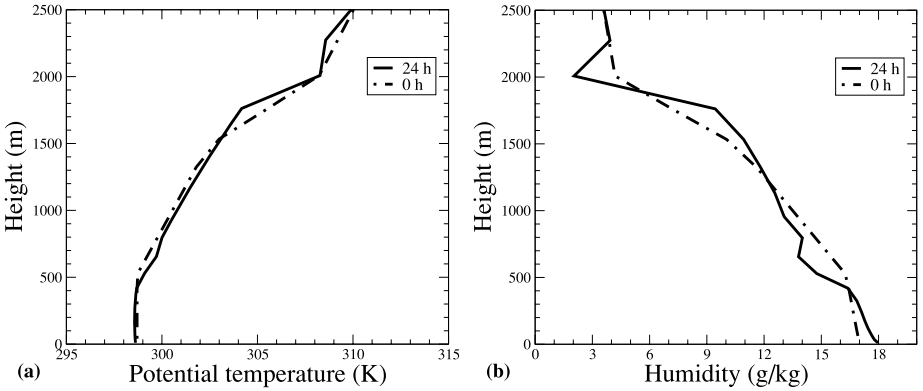

Fig. 4. Vertical profile of potential temperature (a) and specific humidity (b), at the beginning of the simulation and 24 h later.

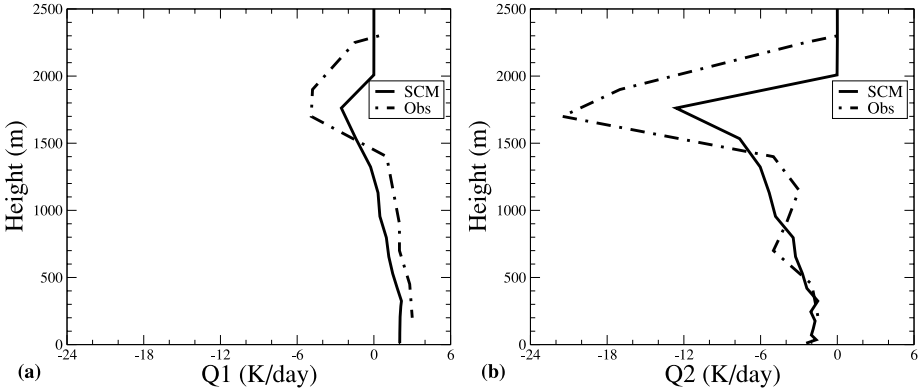

Fig. 5. Apparent heat source (a) and moisture sink (b) of observation and SCM, averaged between 5 and 24 h of simulation.

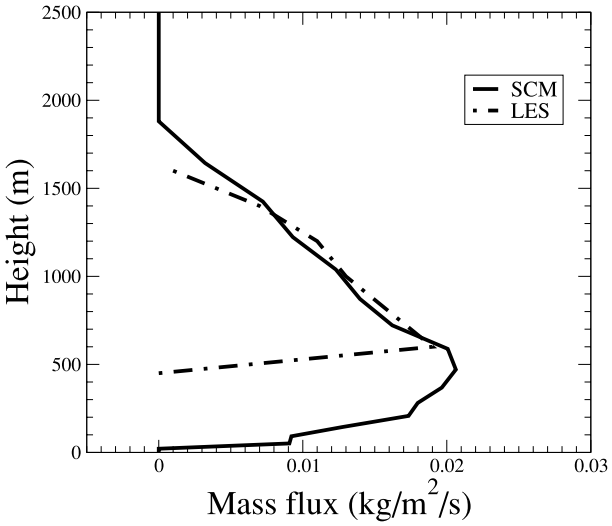

Fig. 6. Vertical profile of the simulated mass flux of SCM (averaged between 5 and 24 h) and reference LES.

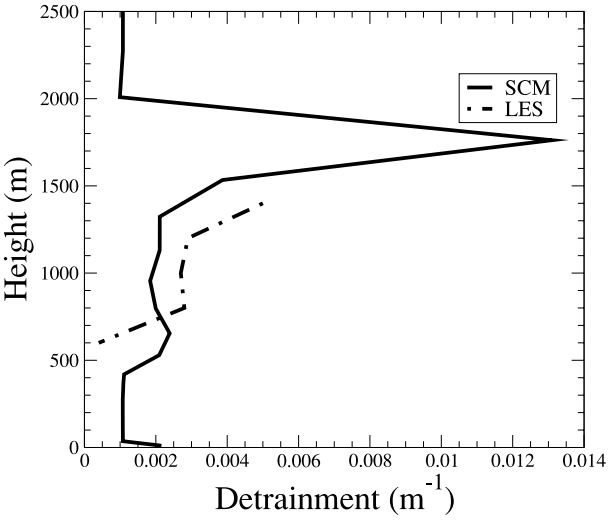

Fig. 7. Vertical profile of the simulated detrainment of SCM (averaged between 5 and 24 h) and reference LES.

and detrainment, the two parametrized variables entering into the formulation of the convective tendency (eq. 14–17). Figure 6 shows the vertical profile of the simulated mass flux (averaged between 5 h and 24 h) superimposed on a reference mass flux from an LES run (SC95). The mass flux reaches its maximum value around the cloud base and decreases until the top of the cloud is reached. In the dry layer, the mass flux follows the convective vertical velocity (not shown); the LES mass flux is equal to zero because it is only defined in the cloud layers (in the presence of condensate). Above the cloud base, the convective vertical velocity continues to increase but the decrease of the convective fraction overcomes it, giving rise to a decrease of the mass flux. This effective decrease in the convective fraction is caused by a rather large value of the detrainment (larger than the entrainment) at this level (as depicted in Fig. 7), according to eq. (31). This large value of the detrainment is a consequence of the use of the buoyancy-sorting model (eq. 29), which allows such large values in the presence of a rather dry environment above the cloud base (typical of the trade wind region). Nevertheless, the simulated detrainment is weaker than that of the LES (Fig. 7) above the cloud base, which explains the lack of moistening mentioned previously.

Finally, the last case, set up by Guichard et al. (2004), hereafter called G04, provided an opportunity to evaluate the convective scheme over an entire continental diurnal cycle (from the build-up of the dry PBL in the morning to deep precipitating convection in the afternoon). The design of this idealized case study was derived from an ARM continental situation (southern Great Plains of the United States) of June 1997 (Xie et al., 2002). The initial condition and the prescribed forcings are shown in fig. 1 of G04, corresponding to a starting time of 5 h local time. The initial profile is quite dry in the free atmosphere, typical of a continental environment, compared to the TOGA-COARE case. The main forcings of this case study are the surface heat fluxes provided every 30 mn in order to obtain a precise diurnal evolution. The sensible heat flux reaches 120 W m^{-2} at around 11 h, and the latent heat flux rises to 400 W m^{-2} 1 h later. The large-scale vertical motion taken into account as a dynamical forcing (from ARM analysis) is rather weak, giving rise to local extrema of large-scale cooling and moistening of less than 6 K d^{-1} and 2 g kg^{-1}, respectively. The wind is prescribed during the simulation and is weak (of the order of 5 m s^{-1} in the lower troposphere during daytime). A grid mesh of 325 km (which corresponds to the size of the ARM analysis) was taken for the definition of the convective time response, following eq. (35).

Figure 8(a) shows the time evolution of the simulated cloud fraction over a 15-h period, covering the convective diurnal evolution. The first very shallow cumulus appear at around 0930 h, that is, 90 mn before what is simulated with the CNRM CRM, according to fig. 4(a) of G04. Nevertheless, the cloud base is located at the correct level (pressure below 900 hPa). Half an hour later, the convective cloud builds up until the 350 hPa level is reached after 5 h. This characteristic time is well reproduced by the convective scheme compared to the CRM simulation but the cloud top appears to be lower by 100 hPa. Between 1600 h and 1830 h, the cloud top is lower, being located at the 525 hPa level, while the CNRM CRM simulates an anvil which persists at least until the end of the day. It is worth noting that it appears to be quite difficult for an SCM to produce an anvil for this case study, considering that the majority of the SCMs used in G04 were not able to simulate such a feature [see fig. 13(b) of G04]. The SCM-simulated cloud vanishes at 1830 h, that is, 1 h later than the average time of the SCMs used in G04. The impact of having a stationarized version of the convective vertical velocity equation (eq. 24) is illustrated in Fig. 8(b). The overall pattern of the cloud fraction is the same as the one depicted in Fig. 8(a)

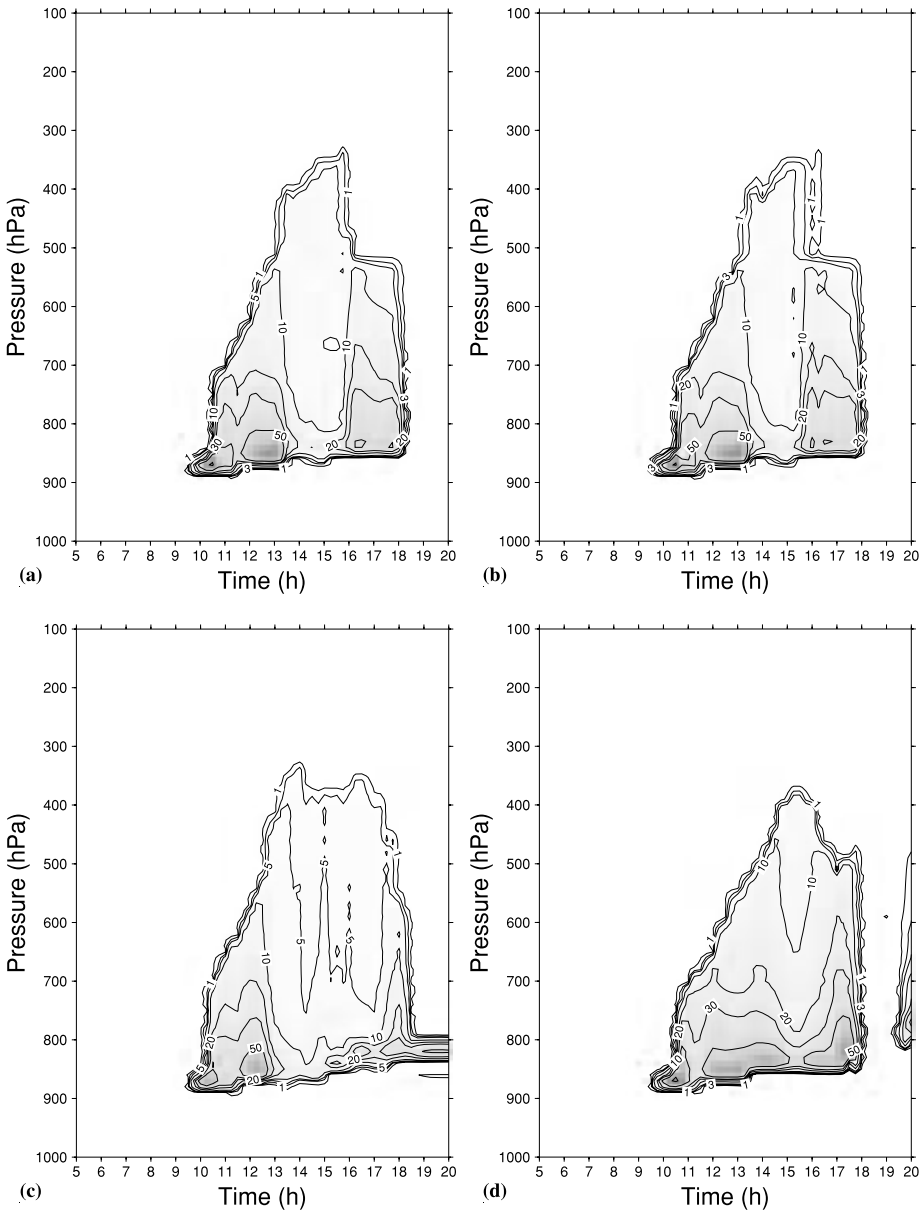

Fig. 8. Cloud fraction time evolution over 15 h of simulation. Control SCM run (a), SCM runs with stationarized convective velocity (b), $\omega_{cn} = -32\,\mathrm{Pa\,s^{-1}}$ (c) and $\omega_{cn} = -44\,\mathrm{Pa\,s^{-1}}$ (d).

but, as expected, it appears more noisy in its time evolution. The sensitivity to parameters entering into the formulation of the turbulent entrainment rate (eq. 25) was also evaluated. Figures 8(c) and (d) again show the cloud fraction time evolution but for simulations using $\omega_{cn} = -32\,\mathrm{Pa\,s^{-1}}$ and $\omega_{cn} = -44\,\mathrm{Pa\,s^{-1}}$, respectively (i.e. 15% around actual value of this parameter) . As expected, when the absolute value of the convective velocity at which the entrainment reaches its minimum is reduced (first case), the convective cloud builds faster, the maximum height being simulated 2 h earlier. In the opposite situation (second case), the convective cloud building is slower; the maximum height is reached at the same time as for the control experiment (Fig. 8a), but the cloud depth is smaller. The CAPE is not sufficiently consumed by the convection as a new cloud appears after 1900 h. The time evolution of the SCM- and CRM-simulated precipitation is shown in Fig. 9. As for the cloud fraction, the SCM starts precipitating an hour and a half before the CRM, at 1030 h. This time lag is less than the average time lag of 3 h obtained by the SCMs participating in G04 (see Fig. 3a of this paper). Apart from this positive time difference, the SCM precipitation rate follows that of the CRM, giving a maximum value of around 9 mm $\mathrm{d^{-1}}$ 5 h after the beginning of rain. In

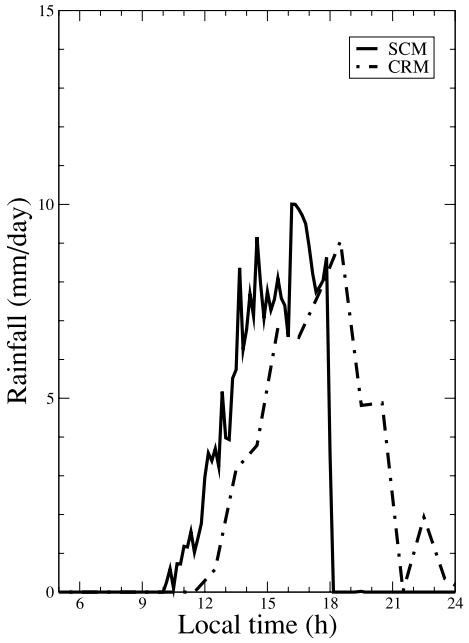

Fig. 9. Precipitation time evolution over 19 h of simulation.

the SCM, the precipitation stops just after 1800 h but the CRM keeps raining until 2400 h due to the development of the anvil mentioned earlier.

Figures 10(a) and (b) show the time evolution of the apparent heat source (Q1) and apparent moisture sink (Q2), respectively, averaged in the free atmosphere (between 800 and 100 hPa). In this layer, Q1 and Q2 essentially include the effects of the convective scheme (plus the radiative scheme in Q1). After 0930 h, Q2 starts with negative values, meaning moistening, in advance compared to the CRM, consistent with what was mentioned in the previous paragraph. Until just after 1300 h, the free atmosphere is moistened by the convective process (i.e. moisture detrainment is larger than the compensating subsidence drying), and cooled through radiative and evaporative detrainment effects. Then, between 1300 h and 1530 h, a new regime is set up. This new regime is characterized by coupled heating/drying of the free atmosphere, which is the consequence of the subsidence term becoming preponderant in the convective tendencies (as the result of large values of the convective vertical velocity and thus the mass flux). The maximum magnitude of heating obtained with the convection scheme is of the same order as that of the CRM (around 5 K d^{-1}). This fact is a justification a posteriori of the grid mesh value chosen in the formulation of the mass flux (eq. 35). Finally, after 1530 h, convection returns to its initial regime (i.e. coupled cooling/moistening). The main discrepancy between SCM and CRM behaviour is the coupled heating/drying regime produced by the former in the middle of the convective life cycle. The second discrepancy is the premature end of heating obtained in the SCM after 1530 h, already discussed earlier. However, it is worth noting that the Q1 and Q2 time evolutions obtained with another CRM (fig. 11 of G04) are closer to our results shown in Fig. 10: a heating/drying regime is simulated between 1530 h and 1700 h, and the heating period is shorter than that obtained with the CNRM CRM. Finally, the present convection scheme is an improvement on the majority of SCMs used in G04, which gives rise to the coupled heating/drying regime throughout the convective life cycle. Figure 11 shows the

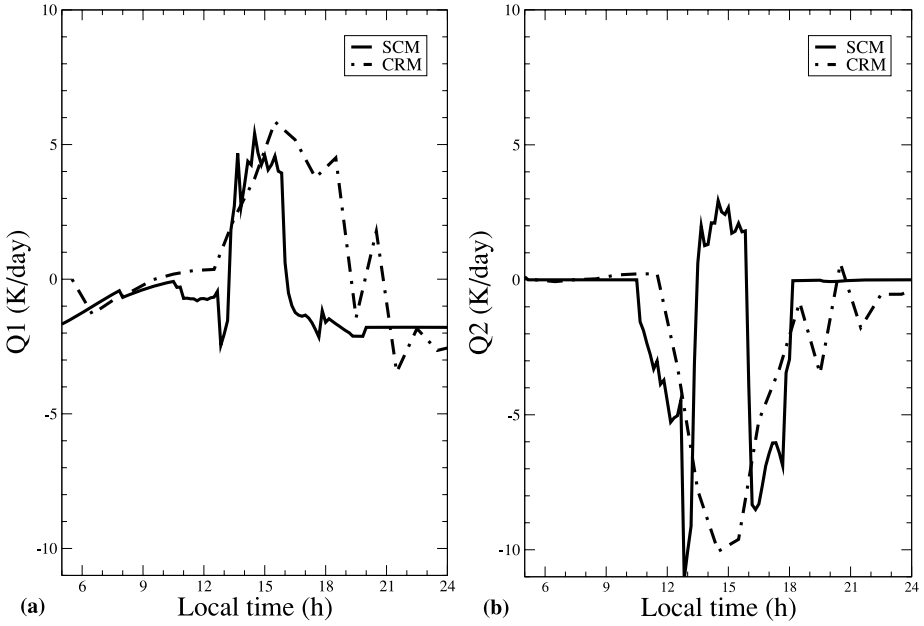

Fig. 10. Apparent heat source (a) and apparent moisture sink (b) time evolution over 19 h of simulation.

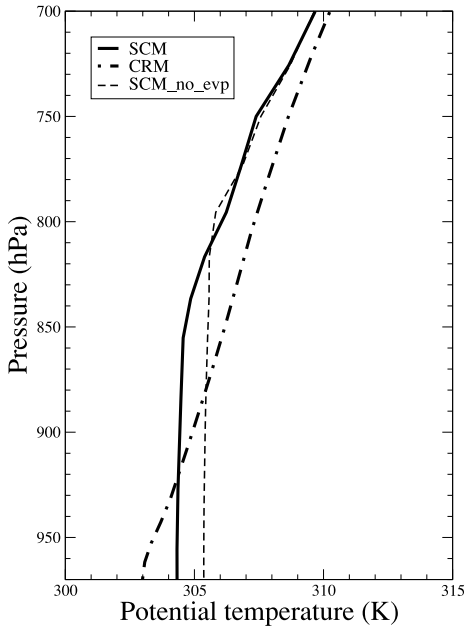

Fig. 11. Potential temperature vertical profile at 1800 h for the SCM with (full line) and without (dashed line) the effect of the evaporation of precipitation, and the CRM (dashed-dotted line).

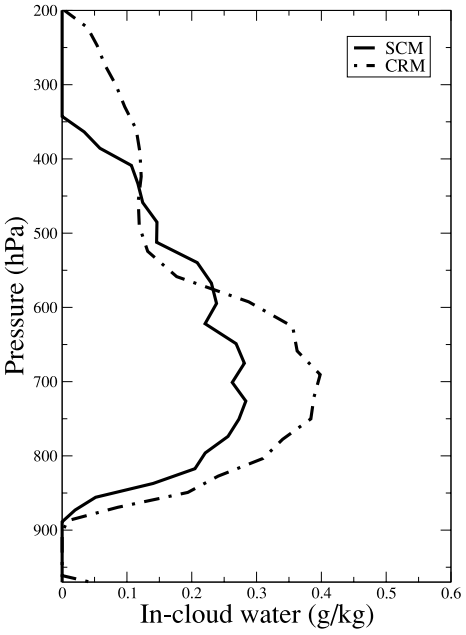

Fig. 12. Vertical profile of the in-cloud water (time averaged between 0600 h and midnight).

potential temperature vertical profile at 1800 h for the SCM (with and without the effect of the evaporation of precipitation) and the CRM. First of all, the SCM profile is more homogeneous than that of the CRM. This is certainly due to the rather strong impact of the downdraughts in the CRM simulation. A large majority of the SCMs used in G04 present a well-mixed profile below 875 hPa (fig. 6(c) of G04). Secondly, at 700 hPa the SCM negative bias is reasonable, being less than 1 K in absolute value, while it is positive for most SCMs used in G04 and larger than 1.5 K as a consequence of the overestimated heating in these SCMs (as mentioned in the previous paragraph). Thirdly, the impact of the evaporation of precipitation appears clearly in Fig. 11. This process accounts for a 1 K cooling of the PBL, which enables reasonable values of the potential temperature to be found in this layer.

The vertical profile of the in-cloud water (time averaged between 0600 h and midnight) is depicted in Fig. 12. The convective in-cloud water is computed from eq. (22) in the present scheme. It is noteworthy that the vertical shape given by the SCM is very similar to the one obtained by the CRM. The maximum value at around 700 hPa tends to be underestimated by 30%, partly due to a longer CRM cumulus life cycle. Secondly, above 400 hPa, the SCM, being unable to reproduce an anvil, underestimates the in-cloud water. However and once again, in comparison to the other SCMs used in G04, the present convective scheme provides better results for both the shape and the magnitude of this field (see fig. 14(c) of G04).

3.2. GCM results

Beyond the one-dimensional validation, the performance of the new convection scheme was assessed in global climate mode. The model used in the previous section is now considered in a three-dimensional global geometry. As mentioned, this model is called AC. Version 5 was used, based on the dynamical core of ARPEGE-IFS (cycle 32), IFS being the global model used at the European Centre for Medium-Range Weather Forecasts (ECMWF). This version is scientifically very close to a previous one (Gibelin and Déqué, 2003). It is a spectral AGCM using a linear Tl127 truncation, a reduced 256 by 128 Gaussian grid and 71 vertical levels (coarser discretization from the 91 levels above 185 hPa, 27 levels instead of 47, the last level being at 0.1 hPa). The dynamical core uses a semi-implicit, semi-Lagrangian, two-time level discretization scheme (time step of 7.5 mn). In the current version of AC described in this paper, the physics (turbulence, microphysics and convection—see details in the SCM subsection) has been changed compared to the 'standard' physics considered in Gibelin and Déqué (2003) and used for the IPCC AR4.

A 20-yr coupled simulation was carried out in order to determine the climate of the model with the new set of parametrizations and to compare it to the observed climate. The ocean model was NEMO (Madec, 2008) in a 2° horizontal resolution and 31 vertical levels. Sea ice is also taken into account in the present version of the ocean model. The simulation started from an initial balanced state of the atmosphere, coming from a 1-yr run forced by climatological SSTs (corresponding to the last decades of the previous century) and from rest in the ocean. The first step of the

validation consisted of analysing global annual mean budgets. The first budget to be considered was the top of the atmosphere energy budget, which corresponds to the vertically integrated energy budget of the atmosphere-ocean-continent system. There are two terms, the net short-wave radiation flux (incoming radiation minus the albedo contribution) and the outgoing long-wave radiation (OLR) flux, which must be balanced. Satellite observations over a period covering more than 10 yr indicate that the OLR is 235 W m^{-2} (Kiehl and Trenberth, 1997). It is worth noting that more recent satellite observations from the years 2000 to 2004 have provided updated values of OLR reaching 238.5 W m^{-2} (Trenberth et al., 2009). Nevertheless, for the purposes of this paper, the older OLR estimate was kept and the value of the characteristic time of the solid auto conversion of the stratiform precipitation scheme (Lopez, 2002) was tuned to reach this amount. The actual value obtained in the present simulation was 234.4 W m^{-2}. In order to close the budget, the characteristic time of the liquid auto conversion of the stratiform precipitation scheme was tuned to finally obtain a net short-wave radiation flux of 234.9 W m^{-2}. The second budget to be considered is the surface energy budget, which corresponds to the ocean–continent vertically integrated energy budget. The net short-wave radiation flux (incoming flux) must be balanced by the sum of the net long-wave radiation flux, and sensible and latent heat fluxes (outgoing fluxes). Having obtained a top energy balance at around 235 W m^{-2} (shown earlier), it appears that the surface energy budget is almost closed, being equal to 0.7 W m^{-2}. In consequence, the atmospheric energy budget is also closed as it is equal to the difference between the top and the surface energy budgets (i.e. $0.5 - 0.7 = -0.2$ W m^{-2}). The actual value of the net short-wave radiation flux is 151.9 W m^{-2} in the present simulation, while the sum of the other fluxes is 151.2 W m^{-2}. The latent heat flux is equal to 86.3 W m^{-2}, the sensible heat flux reaches 17.5 W m^{-2} and the net long-wave radiation flux 47.4 W m^{-2}. All these values are in the range of the known observed or diagnosed values (Kiehl and Trenberth, 1997). The last budget to be considered is the surface water budget, which corresponds to the atmospheric and ocean–continent vertically integrated water budgets. There are two terms, the precipitation and the evaporation fluxes, which must be balanced. The evaporation flux is 3.05 mm d^{-1} (equivalent to a latent heat flux of 86.3 W m^{-2}). The value of the characteristic time of the liquid auto conversion of the convective precipitation scheme (see Section 2.4, remembering that the total amount of auto converted liquid water falls out) was tuned to reach this amount. The actual value obtained in the present simulation was 3.07 mm d^{-1}. It worth noting that all the parameter tuning discussed concerns disposable factors of the microphysics (3 characteristic times of auto conversion). The tuning was performed respecting the range of present knowledge and, importantly, verifying proper behaviour in the SCM simulations (these simulations, reported in the previous section, were performed using the present parameters). Tests using a finer resolution (Tl159, not reported here) showed a rather small sensitivity of the simulated climate to the three tuned parameters mentioned earlier. However, at finer resolutions, a function of resolution might need to be included in the formulation of these parameters. Furthermore, they are supposed to be valid for long-term climate simulations, because they are just factors included in physically sound formulations of the microphysics.

The second step of the GCM validation consisted in comparing the space distribution of seasonal mean averages of some selected fields with their observed counterparts. Two fields were chosen for this purpose, while being relevant in assessing the performance of a convection scheme. First, the zonal mean temperature was considered. This field provides a longitudinally integrated view of the temperature along the vertical, and thus gives an insight into the ability of the convection scheme to redistribute the heating in the vertical direction in the tropics. The reference used was the 44-yr reanalysis data set produced by ECMWF (ERA40, 1958 to 2001; Uppala et al., 2005), but limited to the years 1979–2001. Figure 13 illustrates the zonal mean temperature bias (GCM minus ERA40), for the four seasons. In the tropical tropospheric region, the bias is close to zero except around 30°, in the Hadley cell subsidence region, where it is slightly negative (maximum absolute bias of the order of 1 K, in the middle of the troposphere). It is noteworthy that a slight positive bias appears in the upper troposphere during summer and fall, which is consistent with more intense convection over the continents during these two seasons. The overall small bias provides strong evidence of the proper behaviour of the convection scheme, allowing correct heating of the whole depth of the equatorial troposphere. However, the bias is larger in the stratosphere, with negative values up to –6 K. This particular bias can be much reduced by using a finer vertical resolution in the stratosphere (500 m instead of the 1000 m layer depth considered here; not shown).

The second field considered in the GCM skill assessment was the rainfall amount. This field is relevant in evaluating the convection scheme (in addition to the precipitation scheme embedded in it) insofar as precipitation directly constitutes one of its main outputs (through the condensation process, the second one being the subgrid transport). The reference used was Xie and Arkin (1996). It consists of an analysis of precipitation data from 1979 to 2001, using rain gauge observations, satellite estimates and numerical model predictions. Figure 14 illustrates the precipitation field of both the reference and the GCM, for the summer and winter seasons. The overall global pattern simulated by the GCM is close to that of the reference. The main success of the GCM using the present convection scheme is the rather good reproduction of the two Pacific convergence zones (ITCZ and SPCZ). Unlike what is simulated by the ensemble mean of all the GCMs participating in the IPCC AR4 (Randall et al., 2007), the present GCM is able to obtain an SPCZ (correctly located) distinct from the ITCZ, instead of the 'double ITCZ' over the equator in the former ensemble mean. Nevertheless, the Pacific

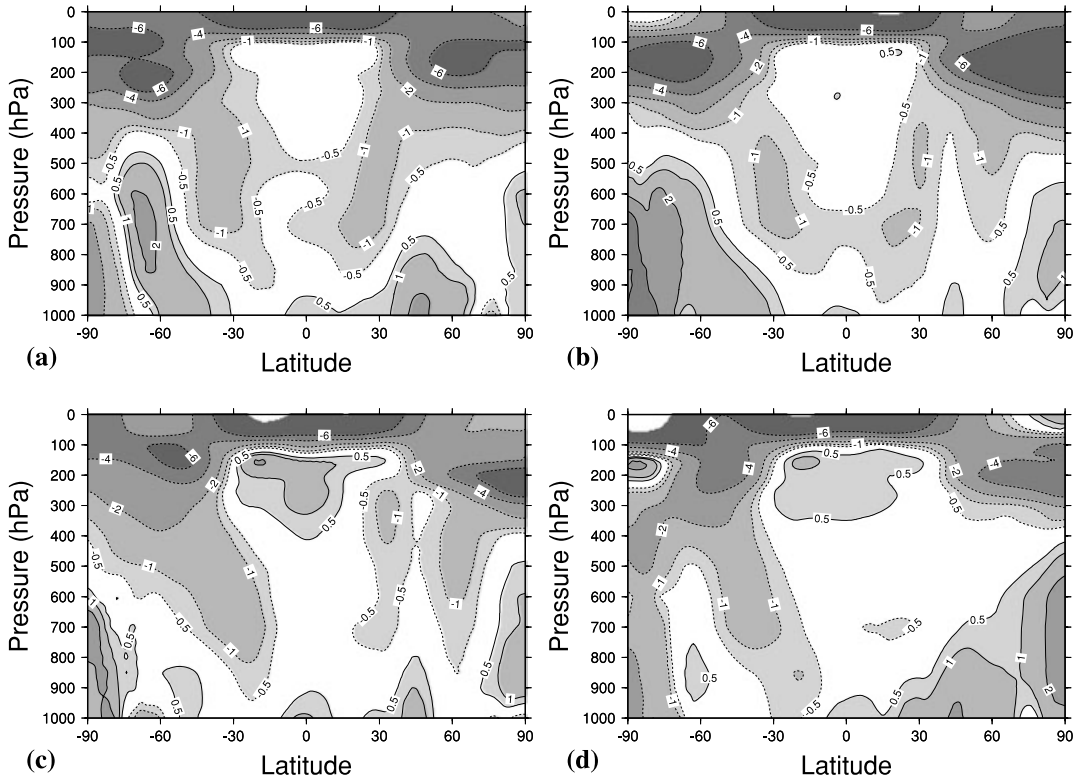

Fig. 13. Zonal mean temperature bias (GCM minus ERA40, in K), DJF (a), MAM (b), JJA (c) and SON (d).

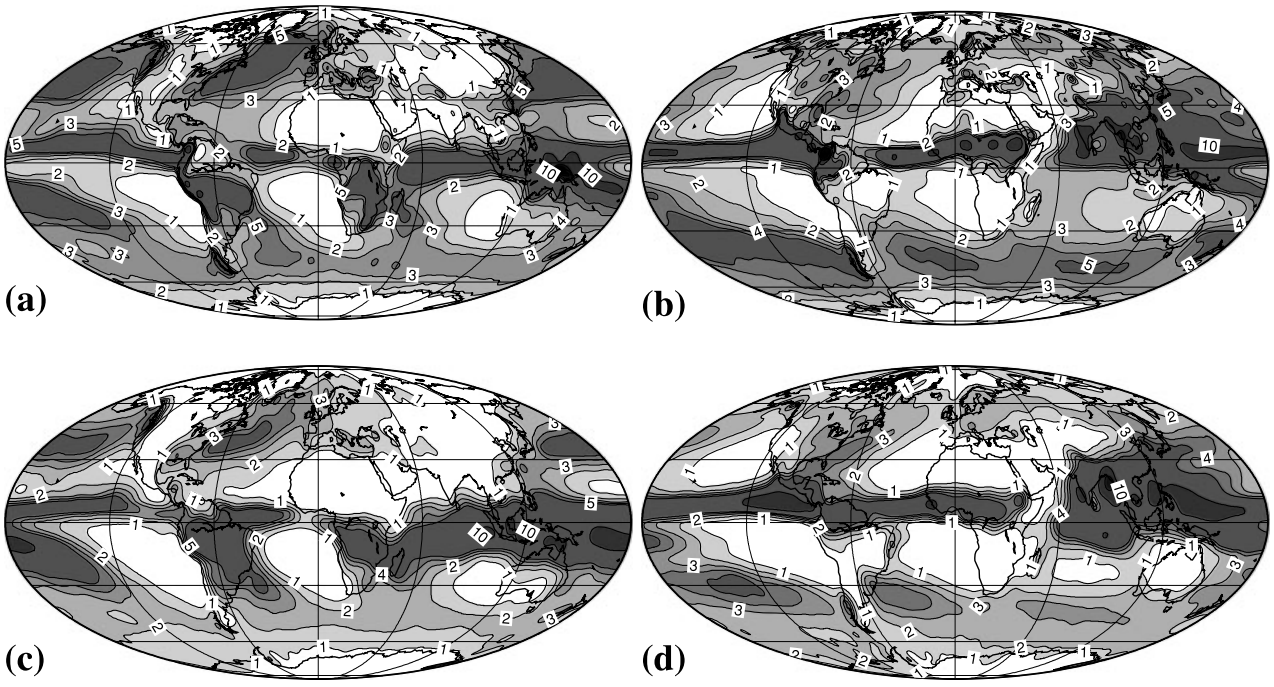

Fig. 14. Precipitation (in mm d^{-1}), DJF GCM (a) and climatology (c), JJA GCM (b) and climatology (d).

equatorial dry zone tends to extend a little too far westwards, which is no longer the case if a higher horizontal resolution is used (Tl159, not shown). Moreover, there are still two main areas of discrepancy. The first is the eastern part of the tropical Indian Ocean, where the GCM gives smaller rain rates in both seasons. In these regions, the trade winds tend to be slightly too strong and mainly less convergent (not shown) giving rise to a reduced activity of deep precipitating convection. The second discrepancy concerns the Sahelian summer precipitation, for which the GCM tends to produce excessive precipitation over the northern part of the Sahel. This might be the result of too low a surface albedo or an incorrect aerosol concentration impacting the short-wave radiative flux [according to a comparison between simulated surface short-wave radiative fluxes and satellite retrievals (not shown)]. Finally, the simulated precipitation in the southern storm tracks appears to be larger than the present reference (Xie and Arkin, 1996). However, in that particular region, these reference rainfall amounts are smaller than those of GPCP (Huffman et al., 1997).

Further to the mean climate assessment previously described, a preliminary climate variability evaluation was undertaken. A significant part of the climate variability is due to equatorial waves (Matsuno, 1966). These waves, being coupled with convection, possibly affect the extra-tropics through westward moving Rossby waves (Gill, 1980). As already reported (Wheeler and Kiladis, 1999; Bechtold et al., 2008), the equatorial wave activity has been evaluated using OLR wavenumber–frequency spectra. The boreal winter season (December–March) was considered for the sake of simplicity. 120 daily OLR values, for a 19-yr period (1979–1997), over a latitude band 15°S–15°N were used for both satellite observation (Liebmann and Smith, 1996) and GCM simulation. The wavenumber–frequency spectra were computed for each year and averaged over the entire period using a methodology described in Céron and Guérémy (1999), which provides spectral densities for both zonal and meridional wavenumbers. In this study, the meridional wavenumber spectral densities were summed in order to consider only the zonal wavenumbers. Following Wheeler and Kiladis (1999), a background spectrum was calculated by successive passes of a 1–2-1 filter in frequency and wavenumber; then, the raw spectra of the symmetric component was divided by the background to obtain an estimate of the signal standing above the 'red' noise. Figure 15 compares these wavenumber–frequency spectra of the observation to the GCM simulations (Tl127 and Tl159). As in Wheeler and Kiladis (1999), the Kelvin and Rossby dispersion curves (approximate for the latter) were superimposed upon the spectra, using three typical tropospheric equivalent depths (12, 25, 50 m). Consistently with Wheeler and Kiladis (1999), the observation spectrum shows three main areas of significant signal: 2 eastward moving oscillations, the Madden and Julian oscillation (MJO) for wavenumbers from 1 to 4 and frequencies from 2 to 4 (30–60 d) and Kelvin waves along their dispersion curves, and one westward moving oscillation corresponding to Rossby waves here again along their dispersion curves. The GCM simulation spectra show rather good agreement with the observation ones. The main discrepancy appears in the MJO signal. The GCM MJO signal is weaker than the observed signal, with a tendency to occur at shorter periods (35 vs. 55 d); the higher resolution GCM simulation (Tl159) exhibits a better signal, both in amplitude and pattern, than its lower resolution counterpart, due to a better representation of tropical convergence zones (not shown) as a consequence of the better resolved wind stress pattern, which is known to be a crucial aspect for coupled GCM. A previous study reported in Lin et al. (2006) has shown the same spectra from 8 yr of IPCC AR4 simulated data. First of all, our spectra appear to be among the best of the 14 GCMs used in the above-mentioned study. Secondly, compared to the CNRM (IPCC AR4 'standard' physics) spectra, a significant improvement is noticeable in terms of both Kelvin and Rossby wave activity, but not really in terms of eastward propagating MJO signal. In order to investigate the MJO activity in greater depth, its variance from observed and simulated (two resolutions) OLR is depicted in Fig. 16. The MJO signal was extracted as in Wheeler and Kiladis (1999), considering wavenumbers from 1 to 4 and frequencies from 2 to 4 (30 to 60 days) for eastward propagating waves only. The observed OLR variance pattern extends from the eastern Indian Ocean to the western Pacific Ocean along 10°S, with a maximum located north of Australia. The simulated OLR variance pattern is rather well located but less elongated in the zonal direction; the variance magnitude is weaker by around 20% than the observed one, which constitutes an interesting result in comparison with the performance of the 14 GCMs used in Lin et al. (2006). Finally, as for the normalized spectra, the higher resolution simulation performed better in terms of raw variance magnitude and pattern, for the MJO signal.

4. Conclusions

A new convection scheme, based mainly on rather simple, already published ideas put together in a consistent way, has been described. The main concept ensuring the consistency of the whole system is buoyancy, a key element of any convective vertical motion. The buoyancy constitutes the forcing term of the convective vertical velocity, which is then used to sequentially define the mass flux, the entrainment and detrainment rates and the convective fraction, and finally the triggering condition. The buoyancy is also used in its vertically integrated form in the formulation of the closure condition. The second originality of the present convection scheme lies in its ability to represent all types of convection, from dry thermals to deep precipitating convective systems, in a continuous manner. This continuous treatment of convection is made possible thanks to the use of a continuous formulation of the entrainment–detrainment rates and CAPE relaxation time, together with an embedded precipitation scheme.

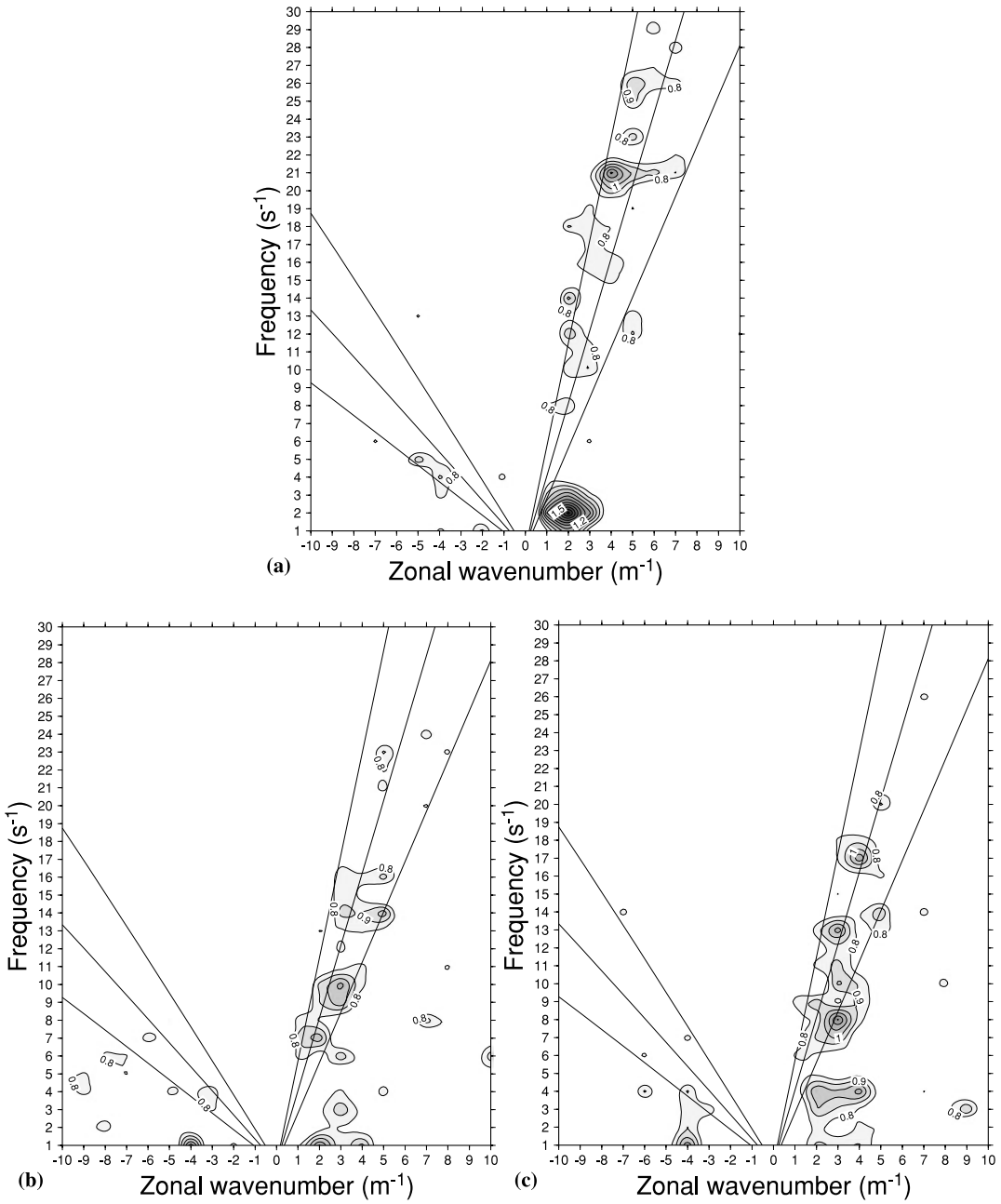

Fig. 15. Normalized space–time spectra (15° S to 15° N, December to March: 120 d, over 20 yr), of satellite-observed OLR (a), GCM Tl127 (b) and GCM Tl159 (c); eastward propagating: left-hand side, westward: right-hand side. Dispersion curves of Kelvin (left-hand side) and Rossby (right-hand side) waves for equivalent depths of 12, 25 and 50 m (from bottom to top).

This new convection scheme has been evaluated in both SCM and GCM modes. First, SCM mode integrations allowed detailed comparisons with observed and explicitly simulated data. The results concerning the deep convection case study (TOGA-COARE) can be summarized as follows. The SCM is able to reproduce the magnitude and vertical shape of the mass flux (as compared to a reference CRM run), indicating proper behaviour of the closure condition, and a proper formulation of the vertical profile of the convective velocity and fraction. Furthermore, the temperature and specific humidity biases after 7 h of simulation are small, and are very similar to those of the best SCMs that participated in a model intercomparison using the present TOGA-COARE case study (Bechtold et al., 2000). Finally, this case study gave the opportunity to show correct behaviour of the downdraughts, giving rise to drying in the very low layers and moistening in the mid levels. Considering the

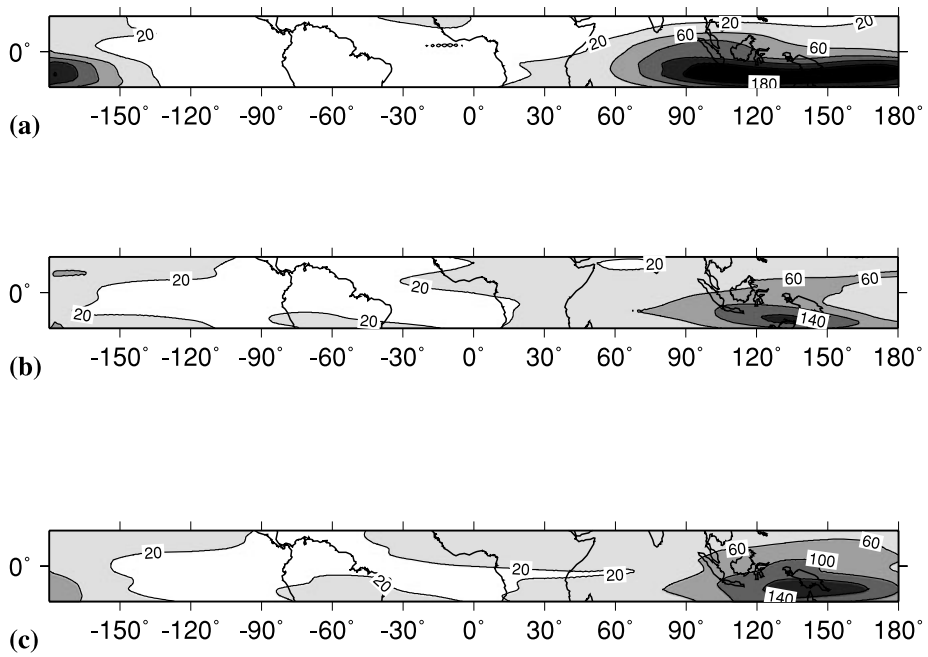

Fig. 16. Variance of OLR (in $W^2\ m^{-4}$) observed (a), GCM Tl127 (b) and GCM Tl159 (c) on the MJO space–time domain.

shallow convection case study (BOMEX), the main conclusions are the following. The convection scheme is able to produce a stationary shallow cumulus with a cloud base at 500 m, a cloud top reaching 1900 m and a cloud fraction decreasing with height from 30 to 10%, in agreement with the observation and LES runs (Siebesma et al., 2003). This case study has also shown the necessity for a minimum vertical resolution to be able to capture the correct cloud pattern. Moreover, the vertical profiles of both temperature and moisture after 24 h of simulation are quite well reproduced, being the consequence of correct mass flux decreasing with height just above the cloud base. Finally, the main findings from the idealized ARM case study are the following. The convective cloud build-up is correctly simulated in time and along the vertical, though it is still 90 mn in advance compared to CRM simulations, that is, half the time difference given by the SCMs participating in Guichard et al., 2004. Furthermore, compared to the same set of SCMs, the present SCM is able to moisten the entire troposphere (at least at the beginning of the convection life cycle), the consequence of correct continuous detrainment in such a rather dry continental environment.

Concerning the evaluation using the ocean coupled GCM mode, the results can be summarized as follows. By means of tuning a few parameters of the microphysics, the basic global budgets are balanced, with values corresponding to the present knowledge of these quantities. The biases in the zonal mean temperature fields are close to zero all along the vertical in the tropical regions for the four seasons, showing the good ability of the convection scheme to provide the correct heating profile over the whole depth of the troposphere. In addition, the overall spatial precipitation pattern is well reproduced in summer and winter, particularly over the Pacific Ocean. The precipitation fields present distinct features for both the ITCZ and the SPCZ, which are located at the correct places. Finally, a preliminary climate variability evaluation has shown that the GCM using the present convection scheme is able to satisfactorily reproduce the space–time spectra of satellite-observed OLR, while giving a smaller variance signal in the MJO domain.

In terms of prospects, the rather simple microphysics embedded in this scheme certainly deserves improvement. One possibility would be to make use of the more detailed scheme of Lopez (2002) (currently taken into account for the large-scale precipitation) instead of the present one from Smith (1990) (used originally for the large-scale precipitation at the time of the development of the convection scheme). Moreover, the location where precipitation evaporation takes place (below the LCL for the time being) is another area where improvements are possible. At the same, there certainly appears to be a need for further validations. In particular, the variability has to be assessed in more detail. This variability assessment will involve a lot of work to cover all relevant time scales, in GCM mode. Diurnal, synoptic intraseasonal and interannual variations must be investigated. Part of this work is currently in progress, in the frame of seasonal forecasting assessment. Coming back to the process study, it would undoubtedly be useful to carry out three-dimensional simulations of documented case studies, as an intermediate step from SCM to GCM mode evaluation. This specific kind of work is also in progress, making use of West African case studies already simulated with a CRM over 1000 km domains. A limited area version of the GCM is considered in order to perform simulations over the same CRM domain and with the same initial

and lateral conditions. Last but not least, it could also be interesting to address the question of the influence of the resolution, using the possibility of variable-mesh simulations with AC as this resolution dependency is set up internally in the convection scheme and has been successfully tested in SCM mode.

5. Acknowledgments

The author is grateful to the people from ENM/UFR, at the early stage of this work, and from CNRM (notably, Drs Pascal Marquet, Isabelle Beau and Françoise Guichard) for their valuable help and discussions throughout the years of development. The author acknowledges the help of Dr. Hervé Grenier who contributed several ideas and suggestions during the development of the scheme, when he was staying at CNRM. He would also like to thank two anonymous reviewers for useful comments and suggestions on an earlier version of the paper.

References

Arakawa, A. 2004. The cumulus parameterization problem: past, present and future. *J. Clim.* **17**, 2493–2525.

Arakawa, A. and Schubert, W. H. 1974. Interaction of a cumulus cloud ensemble with the large-scale environment: Part I. *J. Atmos. Sci.* **31**, 674–701.

Bechtold, P., Redelsperger, J.-L., Beau, I., Blackburn, M., Brinkop, S. and co-authors. 2000. A GCSS model intercomparison for a tropical squall line observed during TOGA-COARE. II: intercomparison of single-column models and a cloud-resolving model. *Q. J. R. Meteorol. Soc.* **126**, 865–888.

Bechtold, P., Köhler, M., Jung, T., Doblas-Reyes, F., Leutbecher, M. and co-authors. 2008. Advances in simulating atmospheric variability with the ECMWF model: from synoptic to decadal time-scales. *Q. J. R. Meteorol. Soc.* **134**, 1337–1351.

Betts, A. K. and Miller, M. J. 1986. A new convective adjustment scheme. Part II: single-column tests using GATE wave, BOMEX, ASTEX, and arctic air-mass data sets. *Q. J. R. Meteorol. Soc.* **112**, 693–709.

Bougeault, P. 1985. A simple parameterization of the large-scale effects of cumulus convection. *Mon. Weather Rev.* **113**, 2108–2121.

Bretherton, C. S., Mc Caa, J. R. and Grenier, H. 2004. A new parameterization for shallow cumulus convection and its application to marine subtropical cloud-topped boundary layers. Part I: description and 1D results. *Mon. Weather Rev.* **132**, 864–882.

Céron, J.-P. and Guérémy, J.-F. 1999. Validation of the space–time variability of African easterly waves simulated by the CNRM GCM. *J. Clim.* **12**, 2831–2855.

Chen, D. H. and Bougeault, P. 1992. A simple prognostic closure assumption to deep convective parameterization: I. *Acta Meteorologica Sinica* **7**, 1–18.

Cuxart, J., Bougeault, P. and Redelsperger, J. -L. 2000. A turbulence scheme allowing for mesoscale and large-eddy simulations. *Q. J. R. Meteorol. Soc.* **126**, 1–30.

Donner, L. J. 1993. A cumulus parameterization including mass fluxes, vertical momentum dynamics, and mesoscale effects. *J. Atmos. Sci.* **50**, 889–906.

Emanuel, K. A. 1991. A scheme for representing cumulus convection in large-scale models. *J. Atmos. Sci.* **48**, 2313–2335.

Geleyn, J.-F., Bazile, E., Bougeault, P., Déqué, M., Ivanovici, V. and co-authors. 1994. Atmospheric parametrisation schemes in Météo-France's ARPEGE N.W.P. model. ECMWF Seminar 94: Physical Parametrisations in Numerical Models, 385–402.

Gibelin, A.-L. and Déqué, M. 2003. Anthropogenic climate change over the Mediterranean region simulated by a global variable resolution model. *Clim. Dyn.* **20**, 327–339.

Gill, A. E. 1980. Some simple solutions for heat-induced tropical circulation. *Q. J. R. Meteorol. Soc.* **106**, 447–462.

Gregory, D. and Rowntree, P. R. 1990. A mass flux convection scheme with representation of cloud ensemble characteristics and stability-dependent closure. *Mon. Weather Rev.* **118**, 1483–1506.

Guichard, F., Petch, J. C., Redelsperger, J.-L., Bechtold, P., Chaboureau, J.-P. and co-authors. 2004. Modelling the diurnal cycle of deep precipitating convection over land with cloud-resolving models and single-column models. *Q. J. R. Meteorol. Soc.* **130**, 3139–3172.

Huffman, G. J., Adler, R. F., Arkin, P., Chang, A., Ferraro, R. and co-authors. 1997. The Global Precipitation Climatology Project (GPCP) Combined Precipitation Dataset. *Bull. Am. Meteorol. Soc.* **78**, 5–20.

Jorgensen, D. P., Le Mone, M. A. and Trier, S. B. 1997. Structure and evolution of the 22 February 1993 TOGA-COARE squall line: observations of precipitation, circulation, and surface energy fluxes. *J. Atmos. Sci.* **54**, 1961–1985.

Kain, J. S. and Fritsch, J. M. 1990. A one-dimensional entraining/detraining plume model and its application in convective parameterizations. *J. Atmos. Sci.* **47**, 2784–2802.

Kershaw, R. and Gregory, D. 1997. Parameterization of momentum transport by convection – I: theory and cloud modelling results. *Q. J. R. Meteorol. Soc.* **123**, 1133–1151.

Kessler, E. 1969. On the distribution and continuity of water substance in atmospheric circulations. *Met. Mon.* **10**, American Met. Soc., 84 pp.

Kiehl, J. T. and Trenberth, K. E. 1997. Earth's annual global mean energy budget. *Bull. Am. Meteorol. Soc.* **78**, 197–208.

Liebmann, B. and Smith, C. A. 1996. Description of a complete (interpolated) outgoing longwave radiation dataset. *Bull. Am. Meteor. Soc.* **77**, 1275–1277.

Lin, J.-N., Kiladis, G. N., Mapes, B. E., Weickmann, K. M., Sperber, K. R. and co-authors. 2006. Tropical intraseasonal variability in 14 IPCC AR4 climate models. Part I: convective Signals. *J. Clim.* **19**, 2665–2690.

Liu, J. Y. and Orville, H. D. 1969. Numerical modeling of precipitation and cloud shadow effects on mountain-induced cumuli. *J. Atmos. Sci.* **26**, 1283–1298.

Lopez, P. 2002. Implementation and validation of a new prognostic large-scale cloud and precipitation scheme for climate and data-assimilation purposes. *Q. J. R. Meteorol. Soc.* **128**, 229–257.

Louis, J. F. 1979. A parametric model of vertical eddy fluxes in the atmosphere. *Bound. Layer Meteorol.* **17**, 187–202.

Madec, G. 2008. "NEMO reference manual, ocean dynamics component: NEMO-OPA preliminary version". Note du Pole de modélisation, Institut Pierre-Simon Laplace (IPSL), France, No 27 ISSN No 1288-1619.

Manabe, S., Smagorinsky, J. and Strickler, R. F. 1965. Simulated climatology of a general circulation model with a hydrological cycle. *Mon. Weather Rev.* **93**, 769–798.

Matsuno, T. 1966. Quasi-geostrophic motions in the equatorial area. *J. Meteorol. Soc. Japan* **44**, 25–43.

Morcrette, J.-J. 1990. Impact of changes to the radiation transfer parameterizations plus cloud optical properties in the ECMWF model. *Q. J. R. Meteorol. Soc.* **111**, 691–708.

Nitta, T. and Esbensen, S. 1974. Heat and moisture budget analyses using BOMEX data. *Mon. Weather Rev.* **102**, 17–28.

Nordeng, T. E. 1994. Extended versions of the convective parametrization scheme at ECMWF and their impact on the mean and transient activity of the model in the tropics. Technical Memorandum N. 206, ECMWF, Reading, UK.

Randall, D. A., Wood, R. A., Bony, S., Colman, R., Fichefet, T. and co-authors. 2007. Climate Models and Their Evaluation. In: *Climate Change 2007: The Physical Science Basis*. Contribution of Working Group I to the Fourth Assessment Report of the Intergovernmental Panel on Climate. Cambridge University Press, Cambridge, United Kingdom and New York, NY, USA.

Redelsperger, J.-L., Brown, P. R. A., Guichard, F., Hoff, C., Kawasima, M. and co-authors. 2000. A GCSS model intercomparison for a tropical squall line observed during TOGA-COARE. I: Cloud-resolving models. *Q. J. R. Meteorol. Soc.* **126**, 823–863.

Siebesma, A. P. and Cuijpers, J. W. M. 1995. Evaluation of parametric assumptions for shallow cumulus convection. *J. Atmos. Sci.* **52**, 650–666.

Siebesma, A. P., Bretherton, C. S., Brown, A., Chlond, A., Cuxart, J. and co-authors. 2003. A large eddy simulation intercomparison study of shallow cumulus convection. *J. Atmos. Sci.* **60**, 1201–1219.

Simpson, J. 1971. On cumulus entrainment and one-dimensional models. *J. Atmos. Sci.* **28**, 449–455.

Simpson, J. and Wiggert, V. 1969. Models of precipitating cumulus towers. *Mon. Weather Rev.* **97**, 471–489.

Smith, R. N. B. 1990. A scheme for predicting layer clouds and their water content in a GCM. *Q. J. R. Meteorol. Soc.* **116**, 435–460.

Tiedtke, M. 1989. A comprehensive mass flux scheme for cumulus parameterization in large-scale models. *Mon. Weather Rev.* **117**, 1779–1800.

Turner, J. S. 1963. The motion of buoyant elements in turbulent surroundings. *J. Fluid Mech.* **16**, 1–16.

Uppala, S. M., KÅllberg, P. W., Simmons, A. J., Andrae, U., Da Costa Bechtold, V. and co-authors. 2005. The ERA-40 re-analysis. *Quart. J. R. Meteorol. Soc.* **131**, 2961–3012.

Wheeler, M. and Kiladis, G. N. 1999. Convectively coupled equatorial waves: analysis of clouds and temperature in the wavenumber–frequency domain. *J. Atmos. Sci.* **56**, 374–399.

Xie, P. and Arkin, P. 1996. Analyses of global monthly precipitation using gauge observations, satellite estimates, and numerical model predictions. *J. Clim.* **9**, 840–858.

Xie, S., Xu, K.-M., Cederwall, R. T., Bechtold, P., Del Genio, A. D. and co-authors. 2002. Intercomparison and evaluation of cumulus parameterizations under summertime midlatitude continental conditions. *Q. J. R. Meteorol. Soc.* **128**, 1095–1136.

Yanai, M., Esbensen, S. and Chu, J. H. 1973. Determination of bulk properties of tropical cloud clusters from large-scale heat and moisture budgets. *J. Atmos. Sci.* **30**, 611–627.

Zhang, G. J. and McFarlane, N. A. 1995. Sensitivity of climate simulations to the parameterization of cumulus convection in the Canadian Center general circulation model. *Atmos-Ocean* **33**, 407–446.